Journal of Catalysis 272 (2010) 210–219

Contents lists available at ScienceDirect

Journal of Catalysis

journal homepage: www.elsevier.com/locate/jcat

Catalytic reduction of NO by CO over $Cu/Ce_xZr_{1-x}O_2$ prepared by flame synthesis

Runduo Zhang [a,c,*,1], Wey Yang Teoh [b,1], Rose Amal [b], Biaohua Chen [a], Serge Kaliaguine [c,**]

[a] State Key Laboratory of Chemical Resource Engineering, Faculty of Chemical Engineering, Beijing University of Chemical Technology, Beijing 100029, PR China
[b] ARC Centre of Excellence for Functional Nanomaterials, School of Chemical Sciences and Engineering, The University of New South Wales, Sydney, NSW 2052, Australia
[c] Department of Chemical Engineering, Laval University, Québec, Canada G1V 0A6

ARTICLE INFO

Article history:
Received 4 December 2009
Revised 29 March 2010
Accepted 1 April 2010
Available online 13 May 2010

Keywords:
NO reduction
deNO_x
Flame spray pyrolysis
Copper
Ceria–zirconia
DRIFTS

ABSTRACT

Mixed oxides of 4% $Cu/Ce_xZr_{1-x}O_2$ ($x = 0, 0.25, 0.50, 0.75, 1$) were synthesized by flame spray pyrolysis and characterized by N_2 adsorption, XRD, XPS, O_2-TPD and H_2-TPR. The as-prepared catalysts were assessed for the equimolar reduction of NO by CO (3000 ppm each, space velocity 50,000 h^{-1}). Incorporation of Zr^{4+} in the form of solid solution with CeO_2 stabilizes the Cu^+ species, which was in turn beneficial for the initial reductive chemisorption of NO to N_2O. A peculiar low-temperature activity giving 40% N_2 yield was found with the composition of $Cu/Ce_{0.75}Zr_{0.25}O_2$ at 150 °C. This is traced to the low-temperature activation of rapid CO oxidation (as probed by *in situ* DRIFTS), related to the abundance of surface reactive lattice oxygen sites and their high reducibility. At 250 °C and above, a N_2 yield of >85% (and ~100% at 350 °C) was obtained for all Zr-containing catalysts i.e. $Cu/Ce_xZr_{1-x}O_2$ ($x < 1.0$), with essentially no intermediate N_2O detected in the exhaust gas stream. An organonitrogen mechanism is occurring in this case.

1. Introduction

Removal of NO_x from high-temperature combustion exhausts is an important subject, with significant environmental impact. NO_x emission is known for causing acid rain and photochemical smog in urban and industrial areas [1]. Recent advances in internal combustion engines were focused on improving their efficiency, but this is often a trade-off between drive supply and pollutants emission, e.g. NO_x and CO, for a gasoline engine. Owing to the increasingly stringent environmental regulations, the development of new materials as three way catalysts (TWCs) with improved *de*NO_x function becomes necessary.

Among the options available, the use of copper-based catalysts for selective catalytic reduction (SCR) of NO_x is an interesting one, from the viewpoint of cost (i.e. does not involve using precious metals) as well as efficiency. In highly isolated form, copper species provide efficient active sites for NO chemical adsorption and reduction, while larger CuO-like aggregates are believed to be active in oxidizing hydrocarbons [2]. In particular, Cu/ZSM-5 zeolite is a very effective catalyst for NO_x reduction because of the atomic dispersion of active metal [3]. Nevertheless, its poor thermal and hydrothermal stability limit its practical application in automobile catalytic muffler. The narrow pores of zeolites are prone to blockage by carbonaceous and sulfurous deposits, with resulting diffusion limitation. In this regard, oxide-based catalysts would in principle be able to circumvent some of these limitations [4].

Ceria is an attractive support that behaves more than just an observer. In many catalytic reactions, its facile Ce^{4+}/Ce^{3+} redox cycle provides high oxygen storage capacity (OSC) [5]. When doped with Cu^+ ions, ceria acts as highly active *de*NO_x catalysts with high resistance to H_2O and SO_2 poisoning [6]. A major drawback of CeO_2 catalyst lies however in its low sintering temperature, especially under practical auto-exhaust atmosphere. This is however a well-studied problem and over the years, an array of CeO_2-based binary oxides [4,7–11] have been designed to address the sintering problem. Of these, CeO_2–ZrO_2 is perhaps the most intensively studied system. The incorporation of ZrO_2 in solid solution with CeO_2 not only improves the latter thermal resistance, but more importantly its redox capacity. The incorporation of Zr^{4+} lowers the energy for Ce^{4+} reduction, thus enhancing CeO_2 reducibility and its associated oxygen mobility.

Conventional impregnation of Cu entity by wet techniques often results in low dispersion of the active component and in the appearance of large agglomerated CuO clusters, which is detrimental to *de*NO_x activity. Hence, the present work explores the rapid synthesis of novel $Cu/Ce_xZr_{1-x}O_2$ nanocomposites via flame spray pyrolysis (FSP) for potential applications in SCR of NO_x. Besides being a single-step synthesis and yielding ready-to-use catalysts, FSP has other obvious advantages, such as proven

* Corresponding author at: State Key Laboratory of Chemical Resource Engineering, Faculty of Chemical Engineering, Beijing University of Chemical Technology, Beijing 100029, PR China.
** Corresponding author. Fax: +1 418 656 3810/5993.
E-mail addresses: zhangrd@mail.buct.edu.cn (R. Zhang), serge.kaliaguine@gch.ulaval.ca (S. Kaliaguine).
[1] R. Zhang and W.Y. Teoh contributed equally to this work.

0021-9517/$ - see front matter © 2010 Published by Elsevier Inc.
doi:10.1016/j.jcat.2010.04.001

stoichiometric formation of $Ce_xZr_{1-x}O_2$ solid solutions [12] and favorable strong interactions between the highly dispersed active component and that of the functional support [13–15]. The purpose of the present work is not only to assess the *de*NO_x capability of the composite catalysts, but more importantly, it seeks to clarify the structural-performance relationship of the catalyst, where all the components in $Cu/Ce_xZr_{1-x}O_2$ are of functional relevance.

2. Experimental

2.1. Catalysts preparation

A series of 4 wt.% $Cu/Ce_xZr_{1-x}O_2$ (x = 0, 0.25, 0.5, 0.75, 1) mixed metal oxides was synthesized by a one-step FSP technique [16,17]. Copper 2-ethylhexanoate (Sigma–Aldrich) was dissolved in xylene (Riedel de-Haen, 98%) together with the corresponding metal precursor for the respective metal oxide support (cerium 2-ethylhexanoate, Strem, and/or zirconium propoxide, Sigma–Aldrich). The total concentration of Ce + Zr in the liquid precursor was set at 0.5 M in all cases. During FSP, the liquid precursor was fed to the nozzle at a flow rate of 5 mL min^{-1}, where it was dispersed by a surrounding 5 L min^{-1} flow of O_2 (1.5 bar). Combustion of the dispersed droplets was ignited by a surrounding supporting flame (1.5 L min^{-1} CH_4/3.2 L min^{-1} O_2). Fine aerosol nanoparticles leaving the flame were collected on a glass fiber filter (Whatmann GF/D) aided by a vacuum pump (Alcatel SD series). The aerosol nanoparticles were scraped from the filter for direct use as catalyst without further treatment.

2.2. Catalyst characterization

The specific surface area of the as-prepared nanoparticles was determined from nitrogen adsorption equilibrium isotherms (BET) at 77 K using an automated gas sorption system (Micromeritics Tristar 3000) operating in continuous mode. Powder X-ray diffraction (XRD) patterns were recorded using a diffractometer (a Philips X'Pert MPD) and Cu Kα radiation (λ = 1.5406 Å) with a 0.1° step scan from 2θ = 20–90°. X-ray photoelectron (XPS) spectra were recorded using an ESCALAB220i-XL spectrometer (VG Scientific) operating at 2×10^{-9} mbar, using a monochromated Al Kα radiation (1486.60 eV). The binding energies were calibrated with respect to the C 1s energy of incidental graphitic carbon at 284.9 eV. The $Cu_{2p3/2}$ binding energy peak area of CuO standard relative to that of the corresponding satellite peak ($I_{Cu^{2+}}$: I_{sat}) was determined to be 1.89. Based on this calibration, the relative Cu^+ content of $Cu/Ce_xZr_{1-x}O_2$ samples was calculated by subtracting the expected Cu^{2+} (based on the measured Cu^{2+} satellite peak area) from the overlapping $Cu_{2p3/2}$ peak areas at the 928.2–938.6 eV.

Temperature-programmed analysis was carried out using a fixed-bed reactor. Prior to temperature-programmed desorption of O_2 (O_2-TPD), the samples (~50 mg) were exposed to 50 mL min^{-1} of 10% O_2/He held at 500 °C for 1 h. The samples were then cooled down to room temperature under the same gas flow. Physisorbed O_2 was eliminated by a 20-mL min^{-1} He purge for 40 min. TPD was conducted by flowing 20 ml min^{-1} of He with temperature ramping at 10 °C min^{-1}. O_2 signal was simultaneously detected and recorded online using a mass spectrometer (MS, Balzers) at m/z of 32. As for temperature-programmed reduction by hydrogen (H_2-TPR), the samples were reduced under 50 mL min^{-1} of 5% H_2/Ar along with temperature rising up to 900 °C at a 5 °C min^{-1} ramping rate. The H_2 consumption in effluent was monitored by thermal conductive detector (TCD).

In situ diffuse reflectance infrared Fourier transform spectra (DRIFTS) were recorded on a FTIR spectrometer (Bruker TENSOR 27) equipped with a high-sensitive MCT detector cooled by liquid N_2. The DRIFTS cell (Harrick) was fitted with KBr windows and a heating cartridge that allowed samples to be heated to 400 °C. The pure samples were dried at 120 °C for 5 h before DRIFTS measurements to eliminate the physisorbed water and finely ground in a ceramic crucible. Prior to each spectrum recording, the sample was flushed in a 20 mL min^{-1} of He for 60 min for background collection and then exposed to a 20 mL min^{-1} of 2% NO, or 2% CO, or 2% NO + 2% CO, balanced in He at the desired temperature. All spectra were measured at the respective temperatures and under continuous flow of gas, with resolution of 4 cm^{-1} and accumulation of 100 scans.

2.3. Catalyst testing

The catalytic activity evaluation of about 100 mg $Cu/Ce_xZr_{1-x}O_2$ catalysts for CO + NO reaction was performed in a fixed-bed reactor under an atmosphere of 3000 ppm NO + 3000 ppm CO balanced by He at a total flow rate of 60 mL min^{-1}, corresponding to a gas hourly space velocity of 50,000 h^{-1}. The reactor was heated externally via a tubular furnace regulated by a temperature controller (Omega CN 3240), with a thermocouple inserted in the catalyst bed, over the range of 100–500 °C in steps of 50 °C. Reactant and product contents in the reactor effluent were recorded only after steady state was achieved at each temperature step. Nitrogen oxides (NO and NO_2) were analyzed using a chemiluminescence NO/NO_2/NO_x analyzer (Model 200 AH, API Inc.). N_2O and CO gases were monitored using a FTIR gas analyzer (FTLA 2000, ABB Inc.). N_2 was analyzed with a gas chromatograph (GC) (Hewlett Packard 5890) equipped with a TCD and columns of molecular 13 X (45–60 mesh, 2.4 m) combined with Silicone OV-101 (100–120 mesh, 0.6 m) operating at an oven temperature of 30 °C.

3. Results and discussion

3.1. Crystallite and surface characterization of $Cu/Ce_xZr_{1-x}O_2$

As-prepared mixed oxides of 4% $Cu/Ce_xZr_{1-x}O_2$ were synthesized rapidly in a direct flame spray pyrolysis (FSP), showing composition-dependent specific surface areas of 68–88 m^2 g^{-1} (Fig. 1). In the absence of Zr component, i.e. Cu/CeO_2, X-ray diffraction

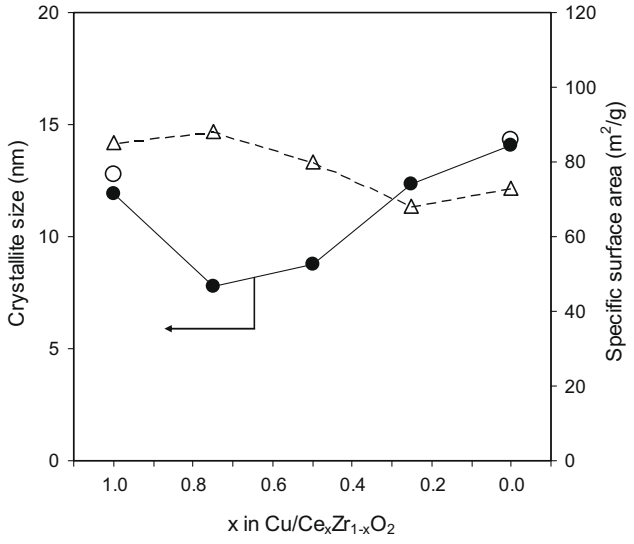

Fig. 1. Scherrer-determined crystallite size (solid circle) and specific surface area (open triangle) of 4% $Cu/Ce_xZr_{1-x}O_2$ as a function of increasing Zr content. Also shown are the crystallite size of similarly prepared pristine CeO_2 and ZrO_2 (open circle).

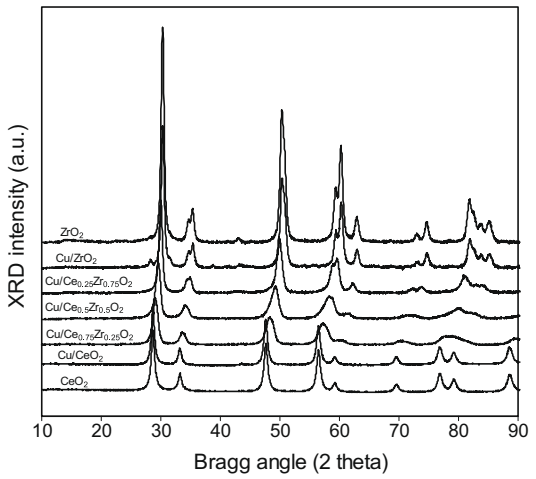

Fig. 2. XRD patterns of as-prepared CeO_2, ZrO_2 and 4% $Cu/Ce_xZr_{1-x}O_2$ (x = 0–1.0).

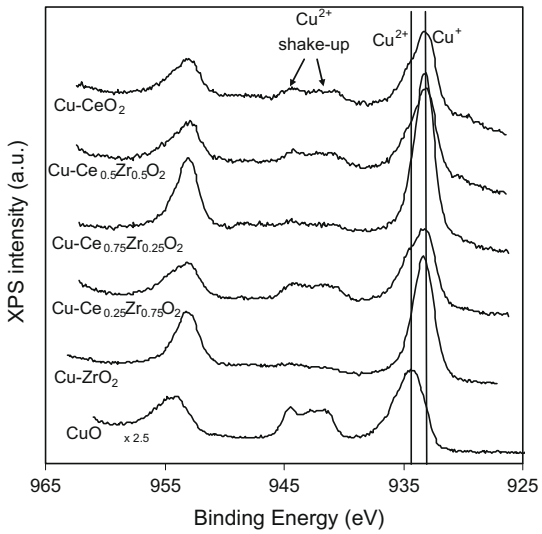

Fig. 3. XPS $Cu_{2p3/2}$ lines of as-prepared 4%$Cu/Ce_xZr_{1-x}O_2$ and that of standard CuO sample.

(XRD) characteristic peaks belonging to well-crystallized cubic phase CeO_2 nanoparticles were obtained, with no peak associated with Cu or any of its constituents detected despite its 4% loading (Fig. 2). This indicates that the Cu phase was well-dispersed as will be confirmed by the surface-sensitive X-ray photoelectron spectroscopy (XPS). It is interesting to note that despite the co-precipitation of both Cu and Ce components during its synthesis, the presence of Cu did not alter the cell parameters of the cubic CeO_2. Similar behavior was also reported for Cu/CeO_2 synthesized by wet precipitation [18], reversed microemulsion [19] and urea–nitrate combustion [20]. Likewise, the crystallite size of CeO_2 (as measured by X-ray line broadening) with and without the presence of Cu was similar, 13 and 12 nm, respectively (Fig. 1). It is only at much higher Cu loadings (>12%) that segregation of small CuO clusters (1–2 nm) could be observed under high-resolution transmission electron microscope[15].

With the addition of Zr component (x = 0.25–1.0), a gradual shift in the Bragg peaks toward higher angle was evident. This corresponds nicely with the formation of cubic phase $Ce_xZr_{1-x}O_2$ solid solutions with no indication of Ce or Zr rich phase segregation detected, while Cu remains XRD invisible. The shift of $Ce_xZr_{1-x}O_2$ Bragg peaks to higher angles with respect to CeO_2 is consistent with a decrease in cell lattice parameters as Zr is incorporated in the lattice [7]. As Ce^{4+} (1.01 Å) has a larger ionic radius than Zr^{4+} (0.80 Å), a longer distance between Ce^{4+} and O^{2-} (d_{Ce-O}) would indeed be expected in the solid solution. As further shown in Fig. 1, the Scherrer-determined crystallite size of $Ce_xZr_{1-x}O_2$ decreases initially to 8 nm with the introduction of Zr (x = 0.75) but increases monotonically as a higher fraction of Zr is introduced (up to 14 nm in Cu/ZrO_2). In the absence of cubic phase stabilization by Ce i.e. Cu/ZrO_2, a predominant tetragonal phase ZrO_2 with a small fraction of monoclinic was observed. The volume fraction of the latter was estimated to be ~0.15 [21]. In the case of pristine ZrO_2, only pure tetragonal phase was formed, as expected from prior FSP studies [12,14].

XPS was adopted to study the speciation and dispersion of Cu (which was invisible under XRD) on the composite catalysts. As shown in Fig. 3, the Cu^{2+} species can be characterized by a $Cu_{2p3/2}$ binding energy of 934.8 eV with a shake-up or satellite peak located at 938.6–948.6 eV, while the corresponding Cu^+ has a binding energy at 933.0 eV [22]. In all cases, the as-prepared catalyst surfaces were Cu enriched, as depicted by the consistently higher value of $(Cu/M)_{surface}$ (open square) relative to $(Cu/M)_{bulk}$ (black triangle), where M = Ce + Zr (Fig. 4). More specifically, Cu is most enriched on the CeO_2 surface with 3.5 times higher surface Cu/M relative to that of the bulk. The addition of Zr gradually lowers the enrichment down to a value of 1.6 times for Cu/ZrO_2, suggesting a higher solid state solubility of Cu in ZrO_2 and/or the strong interactions of the two components, as will be further discussed below.

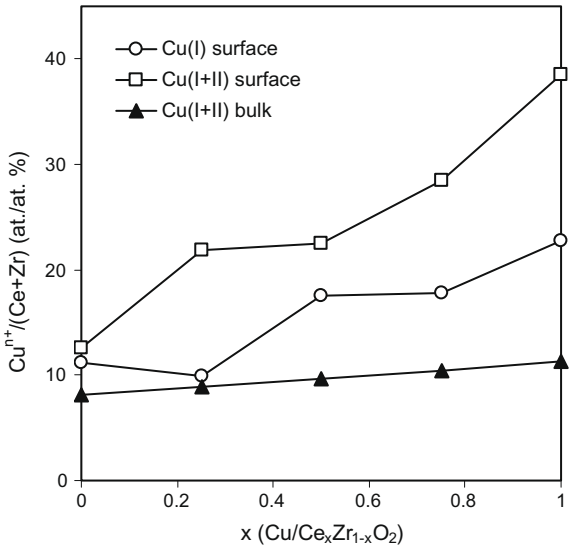

Fig. 4. XPS-determined surface composition of Cu^+ and Cu^{2+} on 4% $Cu/Ce_xZr_{1-x}O_2$ as a function of x. Solid triangles are the theoretical compositions assuming Cu, Ce and Zr form perfect mixed oxide solid solutions.

Among the surface Cu, there exist different fractions of Cu oxidation states across all the different catalyst samples. For quantitative analysis, the relatively close binding energy position of Cu^{2+} and that of Cu^+ would render determination of their relative compositions by conventional XPS peak deconvolution inaccurate. Hence, a more accurate approach is adopted in this instance, by calibrating the relative peak areas of Cu^{2+} to that of the corresponding satellite peak (for more details, please refer to the experimental section). As shown in Fig. 4, although the total amount of copper species ($Cu^+ + Cu^{2+}$) increases with Ce content, the ratio of Cu^+/Cu^{2+} is higher over ZrO_2 support with approximately 89% of the total surface Cu consisting of Cu^+ in the Cu/ZrO_2 sample, while only 60% Cu^+ was found on Cu/CeO_2 surface. Stabilization of Cu^+ in the presence of Zr^{4+} is consistent with the strong interaction

between the two ions which led to lower surface dispersion. It was previously proposed that the facile Ce^{4+}/Ce^{3+} redox cycle could promote the transformation of Cu^{+} to Cu^{2+} involving the following step: $Ce^{4+} + Cu^{+} \rightarrow Ce^{3+} + Cu^{2+}$, and hence resulting in a higher content of Cu^{2+} species in the Ce-containing samples [23]. However, our XPS analysis on the Ce 3d peaks did not detect an appreciable amount of Ce^{3+}, at least within its limit of detection. Surface-dispersed Cu^{+} species is known to be the adsorption site for NO and the formation of intermediate Cu^{+}—NO adsorbed sites is crucial for the activation of the NO molecule [24,25], whereas copper clusters are less active for this *de*NO_x process [26]. Hence, the high percentage of Cu^{+} species over Zr^{4+} may indeed favor catalytic NO reduction as will be discussed below.

3.2. Temperature-programmed desorption (TPD) of O_2

Besides Cu speciation, the state of O species and their quantities are equally important characteristics in the SCR of NO_x. This can be probed by the thermal desorption spectra of oxygen as illustrated in Fig. 5, revealing the presence of α-O_2 i.e. oxygen held on the catalyst surface anion vacancies with a desorption temperature usually below ~700 °C; as well as the β-O_2 desorption which is related to the release of lattice oxygen occurring usually at temperature above 700 °C [27]. Quantification of the deconvoluted peaks of the different desorbed oxygen is summarized in Table 1.

In most cases, the amount of α-O_2 was marginal (<1.5 μmol g^{-1}) with the exception of Cu/ZrO_2, which contained 7.4 μmol g^{-1} of α-O_2. Pristine ZrO_2 alone did not exhibit any appreciable amount of desorbed O_2, suggesting that the presence of α-O_2 in Cu/ZrO_2 to be most likely originating from the anion vacancies created as a result of charge compensation during the substitutional doping of Cu^{+}/Cu^{2+} in ZrO_2 lattice. Even so, the amount of α-O_2 was 5 times lower than that previously observed for perovskite-type mixed oxide of $LaCoO_3$ despite the much lower specific surface area (20–30 m^2 g^{-1}) of the latter [28]. The lower amount of α-O_2 in $Cu/Ce_xZr_{1-x}O_2$ probably concurs with the limited amount of substitutional doping (i.e. low anion vacancies) as reflected by the Cu surface enrichment.

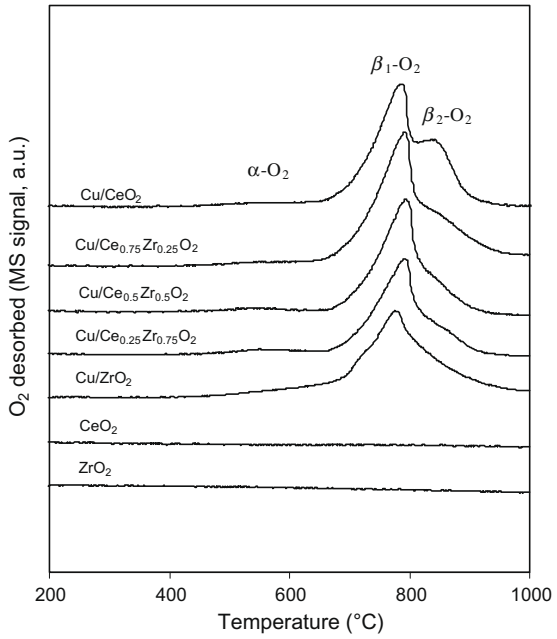

Fig. 5. O_2-TPD of 4% $Cu/Ce_xZr_{1-x}O_2$ as well as similar-prepared pristine CeO_2 and ZrO_2.

Table 1
Amount of O_2 desorbed from $Cu/Ce_xZr_{1-x}O_2$ samples during O_2-TPD experiments.

Sample	Amount of O_2 desorbed (μmol g^{-1})			
	α-O_2	β_1-O_2	β_2-O_2	Total
Cu/CeO_2	1.5 (521 °C)	102.3 (776 °C)	23.4 (848 °C)	127.2
$Cu/Ce_{0.75}Zr_{0.25}O_2$	0.5 (527 °C)	108.1 (780 °C)	15.4 (872 °C)	124.0
$Cu/Ce_{0.5}Zr_{0.5}O_2$	0.8 (527 °C)	91.5 (784 °C)	2.4 (851 °C)	94.7
$Cu/Ce_{0.25}Zr_{0.75}O_2$	1.4 (548 °C)	81.1 (782 °C)	3.7 (857 °C)	86.2
Cu/ZrO_2	7.4 (568 °C)	74.9 (779 °C)		82.3

The amount of β-O_2 increases monotonically with the increase in Ce content: from 75 μmol g^{-1} for Cu/ZrO_2 to 126 μmol g^{-1} for Cu/CeO_2 (Table 1). Two distinct β-O_2 peaks could be observed at ~780 °C (β_1-O_2) and ~860 °C (β_2-O_2), associated with the surface and bulk lattice oxygen bonded to matrix metal ions, respectively. The fact that no β-O_2 was liberated in the case of pristine CeO_2 and ZrO_2 suggests that the lattice distortion induced by the doping with Cu ions lowers the energy for bulk oxygen release [29], although the possibility also exists for provision of oxygen from dispersed Cu. More interestingly, the β_2-O_2 peak, which was not present on Cu/ZrO_2, can be observed to rise as Ce content increases. This is consistent with the general model of facile redox transformation of $Ce^{4+} \rightarrow Ce^{3+}$ in homogeneous solid solution, which results in enhanced bulk lattice oxygen storage and exchange. In the absence of Ce, that is Cu/ZrO_2, only surface lattice oxygen could be liberated, while the bulk lattice oxygen was comparatively less mobile. Such effect of Ce is further exemplified by the H_2-TPR studies presented in the next section.

3.3. Temperature-programmed reduction (H_2-TPR)

The reducibility of $Cu/Ce_xZr_{1-x}O_2$ samples was investigated by quantitative H_2-TPR (Fig. 6, Table 2). In the case of Cu/CeO_2, three reduction peaks at 138 (α-H_2), 153 (β_1-H_2) and 178 °C (β_2-H_2) together with another one appearing at 810 °C were evident in its TPR profile (Fig. 6). The former three peaks are related to the speciation of the supported and highly dispersed Cu [18,20,30,31]. These reduction temperatures are significantly lower than that of the bulk and unsupported CuO, which reduces at ~300 °C [20]. The onset reduction temperature (T_{onset}, temperature at which reduction of catalyst begins) reflects the presence of the most easily reduced Cu species, which in the case of Cu/CeO_2 was determined in our earlier studies to be the CuO dimer at T_{onset} ~ 105 °C [15]. Note also that when compared to our earlier publication [15], the current set of TPR has been optimized to resolve the α- and β_1-H_2, which was previously embedded as a broad hump. For all $Cu/Ce_xZr_{1-x}O_2$ samples containing Ce (x = 0.25–1.0), the T_{onset} was consistently ~105 °C, reflecting the presence of dimeric CuO species, while the T_{onset} ~ 125 °C in Cu/ZrO_2 reflects different and less reducible Cu species. In principle, the speciation of Cu is strongly influenced by the interactions of Cu and the oxide support, and although not shown here, speciation studies on the samples by solid state electron paramagnetic resonance confirmed the gradual transformation from Cu dimers in Ce-rich support toward CuO_x monomers and/or amorphous clusters [32]. While it appears that CuO dimer is present in all the Ce-containing samples, its absolute content changes as a function of Zr content. This is in fact observed with the shifting in α reduction peak toward higher temperature with increasing Zr content.

The β reduction peaks, which are associated with the size of CuO (smaller size yielding lower reduction temperatures) [20], did not change significantly among Ce-containing samples with peak temperatures of β_1-H_2 and β_2-H_2 at ~153 and 177 °C, respectively. This corroborates the XPS analysis that the surface Cu species were of fine and highly dispersed nature. On the contrary,

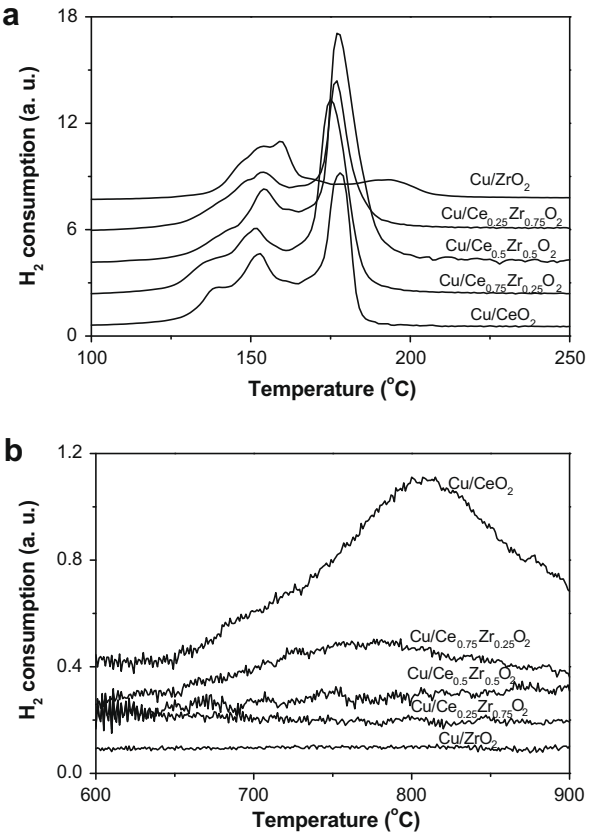

Fig. 6. H_2-TPR of 4% $Cu/Ce_xZr_{1-x}O_2$ (x = 0–1.0) at (a) low temperature and (b) that at high temperature.

the β reduction peaks of Cu/ZrO_2 were shifted to higher temperatures (with β_2-H_2 of 192 °C) as consistent with the relatively lower Cu dispersion and more importantly demonstrates the strong interactions between Cu and Zr. Another distinct difference between the TPR spectra of Cu/ZrO_2- and Ce-containing samples is the lower peak area of β_2-H_2 compared to that of β_1-H_2. This was thought to be related to the poor reducibility to Cu^0 in ZrO_2 matrix and could arise due to a few inter-related reasons: (1) strong interactions between Cu^+ and Zr^{4+}; (2) poor surface Cu enrichment (i.e. dispersion); and (3) the absence of Ce^{4+}/Ce^{3+} redox-assisted reduction of Cu^{n+} species. Except for Cu/ZrO_2, the H_2 consumption related to the reduction of Cu ($\alpha + \beta$) were much higher than the theoretical limit for all the catalysts for complete Cu reduction (Table 2), in agreement with previously reported work on similar systems [18,33]. In the case of Cu/ZrO_2 where no Ce is present, only slightly higher H_2 consumption (373 μmol g^{-1}) than the theoretical value (350 μmol g^{-1}, based on XPS-determined Cu^+/Cu^{2+} compositions) was *measured*. The result strongly implies the occurrence of H spillover effect over reduced surface Cu, reducing some of the Ce^{4+} to Ce^{3+}. The highest reducibility was observed for sample $Cu/Ce_{0.75}Zr_{0.25}O_2$ (sum of α- and β-H_2 of 810 μmol g^{-1}) where it is well established that the substitution of Zr^{4+} in Ce^{4+} increases its oxygen mobility [29], which in this case allows for the easy reduction of the latter.

The bulk capacity of lattice oxygen storage in Cu/CeO_2 (through Ce^{4+}/Ce^{3+} redox) is further evident at elevated temperature around 810 °C (Fig. 6b). The content decreases gradually with the increase in Zr content, as consistent with the trend of β_2-O_2 observed earlier through O_2-TPD. No appreciable amount of high-temperature reduction band could be observed for Cu/ZrO_2, again consistent with the absence of β_2-O_2.

3.4. Catalytic reduction of NO by CO over $Cu/Ce_xZr_{1-x}O_2$

The temperature dependence of catalytic reduction of NO by CO over as-prepared catalysts is shown in Fig. 7a and b. In the absence of Cu, the *de*NO_x activity of pristine CeO_2 was low with ~20% NO conversion (Fig. 7a) to N_2 (Fig. 7b) at 300 °C, while similar values were only observed with pristine ZrO_2 at 500 °C. No intermediate N_2O was formed (Fig. 7c), while equimolar CO and NO conversions were measured over these pristine supports (Fig. 7d), in agreement with the overall stoichiometry: $2CO + 2NO \rightarrow N_2 + 2CO$.

An enhancement in NO conversion was observed over CeO_2 with the addition of 4% Cu, resulting in an initiation at 200 °C and reaching a value of 96% at 400 °C. Here, the initial NO adsorption and decomposition over highly dispersed Cu [24] was deemed as an important step for NO + CO reaction. Improvement in NO conversion is further evident with the addition of Zr i.e. $Cu/Ce_xZr_{1-x}O_2$ ($x < 1$). Compared to Cu/CeO_2, doping of the catalysts with Zr presents some physicochemical advantages: strong interactions of Cu and Zr leading to high Cu^+/Cu^{2+} ratio, where NO chemisorbs preferentially on Cu^+ and enhanced surface oxygen mobility. More specifically, they are beneficial for the intermediate reduction of NO to N_2O (Fig. 7c), where the latter was generated in an expected decreasing order of $Cu/ZrO_2 > Cu/Ce_{0.25}Zr_{0.75}O_2 > Cu/Ce_{0.5}Zr_{0.5}O_2 > Cu/Ce_{0.75}Zr_{0.25}O_2$.

While Cu^+ sites are important for the chemisorption of CO and NO, removal of atomic O (through surface lattice oxygen sites) produced from the decomposition of NO and N_2O requires equal or more rapid oxygen consumption through CO oxidation. Here, CO has a dual role of removing the O while keeping the Cu sites in reduced state. The accumulation of N_2O intermediate below 250 °C suggests the limiting role of O removal, and the similar extent of CO and NO conversions (and the absence of intermediate N_2O) for all catalysts above 250 °C corroborates the mentioned synergistic effect between CO oxidation and NO reduction.

Interestingly, a high 40% N_2 yield was observed at the low temperature of 150 °C for sample $Cu/Ce_{0.75}Zr_{0.25}O_2$ (see Fig. 7a and b). The outstanding low-temperature activity may be attributed to the combination of the abundance of surface lattice oxygen sites and most importantly, the high reducibility of these sites at low temperature (Table 2). As will be shown by *in situ* DRIFTS, the

Table 2
Quantitative analysis of H_2-TPR for $Cu/Ce_xZr_{1-x}O_2$ samples.

Sample	H_2 consumption (μmol g^{-1})				
	α	β_1	β_2	Total	Theoretical[a]
Cu/CeO_2	37 (138 °C)	314 (153 °C)	309 (178 °C)	660	441
$Cu/Ce_{0.75}Zr_{0.25}O_2$	63 (137 °C)	250 (151 °C)	497 (176 °C)	810	435
$Cu/Ce_{0.5}Zr_{0.5}O_2$	34 (141 °C)	226 (155 °C)	538 (178 °C)	798	384
$Cu/Ce_{0.25}Zr_{0.75}O_2$	31 (144 °C)	337 (154 °C)	301 (177 °C)	669	488
Cu/ZrO_2		284 (156 °C)	89 (192 °C)	373	350

[a] Theoretical H_2 consumption calculated based on 4% Cu and the percentage amount of Cu^+ and Cu^{2+}: $CuO + H_2 \rightarrow Cu + H_2O$; $Cu_2O + H_2 \rightarrow 2Cu + H_2O$. *Note*: XPS-determined surface Cu^+/Cu^{2+} composition is assumed here as the bulk composition for each catalyst to allow calculation of these theoretical H_2 consumptions.

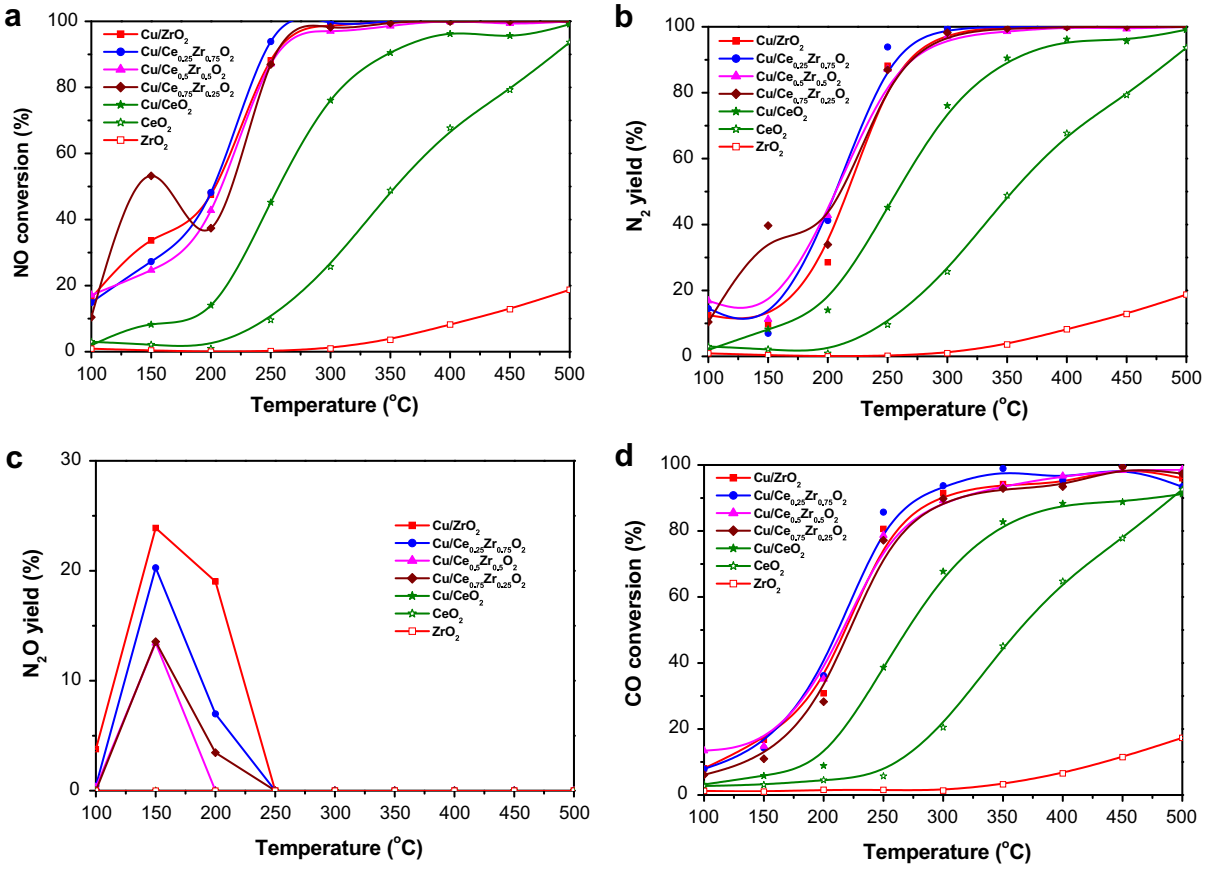

Fig. 7. (a) NO conversion, (b) N_2 yield (c) N_2O yield and (d) CO conversion in CO + NO reaction over as-prepared catalysts. Conditions: GHSV = 50,000 h^{-1}, 3000 ppm NO, 3000 ppm CO.

reducibility of these sites facilitated the rapid O removal (activation of rapid CO → CO_2) at 150 °C.

3.5. In situ DRIFT study

Based on the best performing 4% $Cu/Ce_{0.75}Zr_{0.25}O_2$ (on the basis of N_2 yield at low temperature), the formation of surface species during NO or CO adsorption (and sequential introduction of both) over this catalyst was probed by means of *in situ* DRIFTS (Figs. 8–10). As evident in spectrum (a), the adsorption of 2% NO/He over the catalyst at 300 °C gave rise to several peaks in the range of 1100–1700 cm^{-1}. Adsorption of NO_x on surface Cu exists as configurations of chelating $\left(Cu^{n+}\langle{O \atop O}\rangle N{-}O\right)$ as well as bridging $\left({Cu^{n+}{-}O \atop Cu^{n+}{-}O}\rangle N{-}O\right)$ bidentate nitrate, [33–35] as reflected by the most intense bands of asymmetric stretch (—NO_2) at 1609 cm^{-1} and shoulders at 1621 and 1582 cm^{-1}. Additional bridging nitrates could be formed on the catalyst surface as reflected by the moderate bands at 1213 cm^{-1}, while the N-containing compounds other than nitrate species are marginal [36]. Upon switching to 2% CO/He, the surface *ad*NO_x species were reduced, and hence a distinct change in the DRIFT structure could be seen from spectrum (b) in Fig. 8 except for the now-attenuated bands at 1100–1700 cm^{-1} for nitrate species, which nearly vanished. Instead, the spectrum now consists predominantly of carbonaceous species, with a remarkable band at 1544 cm^{-1} correlated to Cu^{n+}—ν(C=O) of bidentate carbonate species [37,38], while the peaks maxima at 1521 cm^{-1} were ascribed to Cu^{n+}—$\nu_s(COO^-)$ of carboxylates [39,40]. More specifically, the band at 1435 cm^{-1} is likely caused by nitrite species resulting from the partial reduction of nitrates

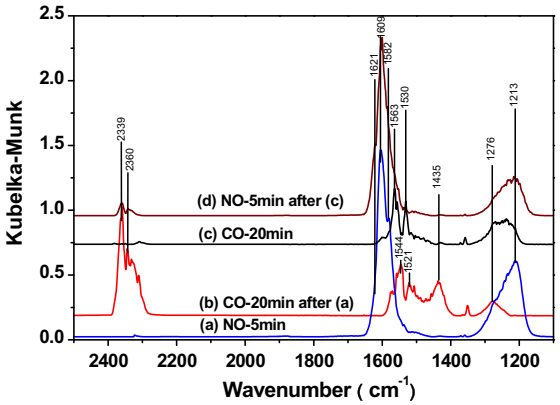

Fig. 8. DRIFT spectra of adsorbates produced from the flow of (a) 2% NO/He for 5 min, (b) 2% CO/He for 20 min after (a), (c) 2% CO/He for 20 min, and (d) 2% NO/He for 5 min after (c) over 4% $Cu/Ce_{0.75}Zr_{0.25}O_2$ at 300 °C.

[34]. The appearance of an intense doublet at 2339 and 2360 cm^{-1} is due to gaseous CO_2. This illustrates the ability of NO-pretreated sample to oxidize CO, which is in fact more active than that over the same catalyst sample without NO pretreatment.

As direct comparison, $Cu/Ce_{0.75}Zr_{0.25}O_2$ was exposed to 2% CO/He at 300 °C without NO pretreatment (spectrum (c), Fig. 8). Here, the carbonaceous-related bands were similar to those of Fig. 8b. On closer inspection, the higher doublet peaks intensity of CO_2 (2339 and 2360 cm^{-1}) and carbonates bands (1544 cm^{-1}) in spectrum (b) of Fig. 8 strongly implies that NO pretreatment is beneficial for the transformation of CO → CO_2 and carbonate. Further exposure of

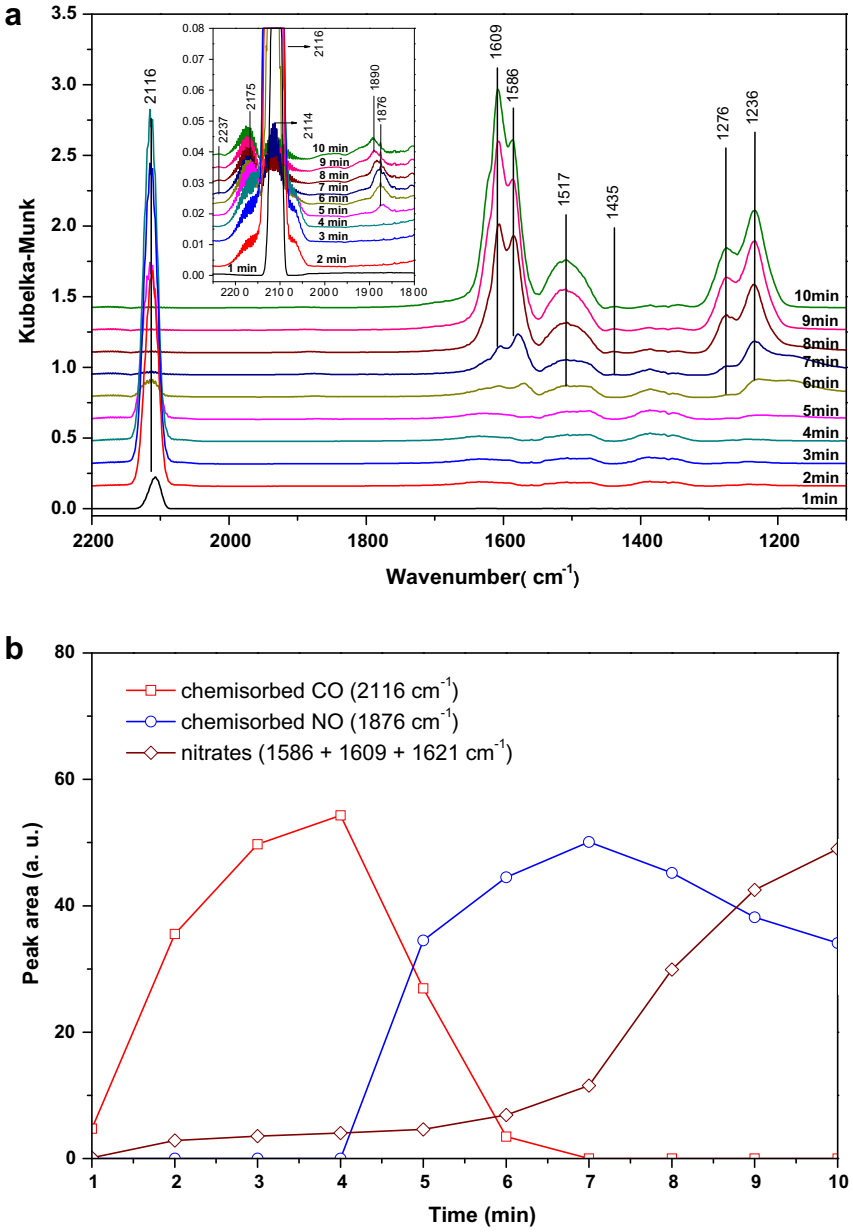

Fig. 9. (a) Dynamic changes of DRIFT spectra of adsorbates produced from the flow of 2% NO/He + 2% CO/He at 50 °C over 4% $Cu/Ce_{0.75}Zr_{0.25}O_2$ as a function of time and (b) time dependence of the integrated areas of the IR peak in the range of 1100–2200 cm^{-1}.

the CO-saturated sample with 2% NO/He at the same temperature (spectrum (d), Fig. 8) resulted in the appearance of bands related to *ad*NO_x species, similar to that of spectrum (a).

To further understand the NO and CO co-interactions, the DRIFT spectra of the catalyst surface were monitored in the presence of the (NO + CO) mixture as a function of time at 50 °C (Fig. 9a), as well as function of temperature from 50 to 400 °C (Fig. 10a). The dynamic changes of the surface coverage of various corresponding species were determined according to a deconvolution of the related spectra with the results being depicted in Figs. 9 and 10b.

At low temperature of 50 °C, NO and CO interacted with the active sites resulting in their simultaneous chemisorptions as evidenced by the DRIFT spectra in Fig. 9a. In line with literature assignment [37], the IR band at 2116 cm^{-1} for chemisorbed CO background with the typical roto-vibrational fringes at 2114 and 2175 cm^{-1} for gaseous CO was initially found. When the adsorption time (t) is extended, the intensity of band at 2116 cm^{-1} for monocarbonyl species passed through a maximum at 4 min before its total disappearance at $t > 7$ min (Fig. 9a and b). The diminution of monocarbonyl is accompanied by the onset of new IR peaks 1876 and 1890 cm^{-1} at $t > 4$ min, attributed to nitrosyl (chemisorbed NO) and physisorbed molecular NO, respectively [41–43]. Hence, it is possible that a competitive adsorption between chemisorbed NO_x and chemisorbed CO for common active sites is occurring, with the latter (especially nitrates) being dominant due to higher thermal stability. This is evident by the strong surface coverage of bidentate nitrates (1236 and 1550–1650 cm^{-1}) and monodentate nitrates (1517 cm^{-1}) at prolonged exposure period $t > 7$ min. Similar findings where CO appears to be more weakly adsorbed than NO was reported over anionic vacancy sites of La(Fe, Co, Mn)$_{1-x}Cu_xO_3$ perovskite-type oxides [44].

Fig. 10a illustrates the DRIFT study of species formed over 4% $Cu/Ce_{0.75}Zr_{0.25}O_2$ at various temperatures. Here, it is evident that gaseous CO_2 (2339 and 2356 cm^{-1} doublet) becomes apparent at

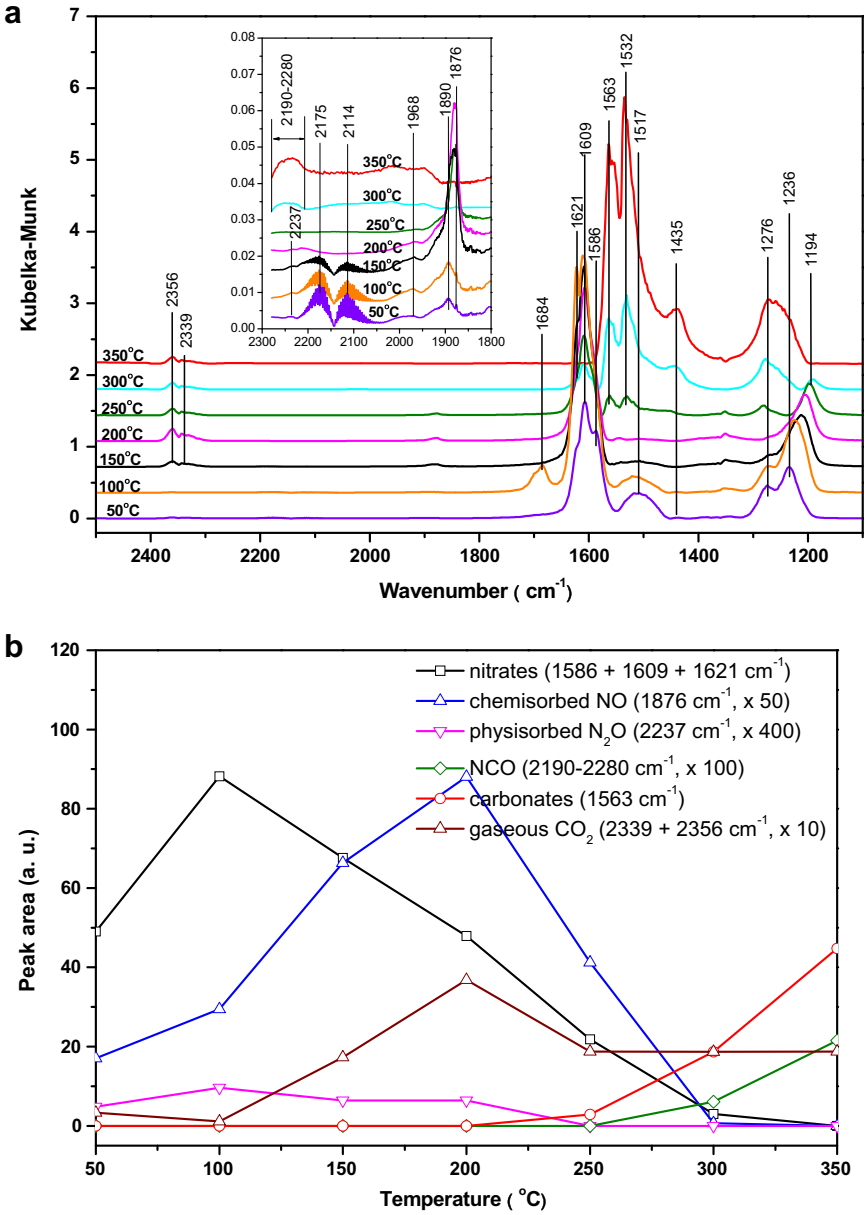

Fig. 10. (a) Dynamic changes of DRIFT spectra of adsorbates produced from the flow of 2% NO/He + 2% CO/He for 5 min over 4% $Cu/Ce_{0.75}Zr_{0.25}O_2$ as a function of temperature and (b) time dependence of the integrated areas of the IR peak in the range of 1100–2500 cm^{-1}.

150 °C, coinciding with the peculiarly high N_2 yield seen earlier in Fig. 7b. The observation provides evidence for the low-temperature activation of the CO oxidation (limiting step). The oxidation of CO is in principle dependent on the removal of O, which is in turn a function of the catalyst reducibility [15]. The onset activation of CO oxidation step results in the corresponding decomposition of surface nitrates (Fig. 10a and b). Careful scrutiny of DRIFT spectra did not detect any trace amount of monocarbonyl species at all temperatures, which was expected due to displacement by nitrosyl as discussed earlier. Hence, the CO_2 generation is possibly realized via an Eley–Rideal mode involving the interaction of chemisorbed nitrate species with the gas-phase carbon monoxide. On the other hand, some minor formation of N_2O intermediate can be detected from the ν(N—N) at 2237 cm^{-1} and ν(N—O) stretching was immersed at 1276 cm^{-1} [41,45] in agreement with the outlet gas analysis during catalytic testing (Fig. 7c).

At 250 °C, a sudden rapid increase in the bidentate carbonate bands 1563 and 1276 cm^{-1} [36], together with that of $\nu_s(COO^-)$ carboxylates at 1532 cm^{-1} grew at the expense of bridging (1586, 1609 and 1621 cm^{-1}) and monodentate (1517 cm^{-1}) nitrates. The lack of ν(N—N) is again in agreement with the absence of N_2O in the outlet gas stream at high temperatures. The growth of a new nitrites band (1435 cm^{-1}) with increasing temperature indicates the occurrence of partial reduction of nitrates to lower the N-valence. Similarly, the bridging nitrate band red-shifted monotonously from 1236 to 1194 cm^{-1} with the increasing temperature from 50 to 300 °C can be attributed to the formation of bridging nitrito species [36,41].

As shown in Fig. 10b, a maximum amount for chemisorbed NO was achieved at 200 °C. Thereafter, the nitrosyl species vanished as the temperature reaches 300 °C. Interestingly, a relatively broad band at 2190–2280 cm^{-1} was discernable at temperature above 300 °C and is likely due to isocyanate (NCO) species [46,47]. The band at 2260–2270 cm^{-1} was previously assigned to isocyanate complex bound to surface metal atoms [48], while the vibration of Cu^+—NCO^- that lies ca. 2200 cm^{-1} belongs to that of Cu^+—NCO

vibration [45]. These isocyanate species are formed following NO dissociation on the metallic surface and subsequent spillover onto the support oxides where they accumulate, whereas a blue shift in the IR band to higher frequency could be seen accompanying with this NCO spillover process [49,50]. Here, it is likely that accumulation of isocyanate arises from the partial reduction of nitrate/nitrite/nitrosyl species at the ceria–zirconia sites, which may be less capable of catalyzing full reduction to N_2 in the absence of vicinal Cu. It is envisaged that the high-temperature activation of CO oxidation at >300 °C provided more reduced ceria–zirconia sites for the partial reduction of nitrate, resulting in the intensification of NCO signal at 2190–2280 cm^{-1} (Fig. 10a and b).

3.6. Mechanistic of CO + NO reaction over $Cu/Ce_xZr_{1-x}O_2$

In general, the proposed *de*NO_x mechanisms reported in the literature can be categorized as redox mechanism as well as the organonitrogen mechanism. The former consists of an initial dissociation–chemisorption NO yielding N_2O intermediate and an oxidized surface, while the role of CO is to further reduce N_2O into the final product of N_2 as well as to restore the initial catalytic surface [44,51]. In contrast, the latter organonitrogen mechanism involves the generation of isocyanate (NCO) compounds as intermediates [52,53]. During an actual catalytic reduction process of NO, more than one reaction mechanism can occur simultaneously, and the relative contribution of each mechanism essentially depends on the catalyst nature, reductant type and reaction conditions (temperature, concentration, etc.) [54–56].

Based on the present *de*NO_x activity and DRIFT results, it can be reasonably deduced that there are a few key aspects of the functional characteristics of $Cu/Ce_xZr_{1-x}O_2$, which are in turn instrumental to assess both redox and/or organonitrogen mechanisms for NO reduction by CO. At low temperatures (50–250 °C), the presence of highly dispersed Cu^+ promotes the direct chemisorption of NO as nitrosyl species (Eq. (1)). At the same time, some oxidation of chemisorbed NO could also take place with the assistance of Ce^{4+}—O^- to form nitrites (Eq. (2)) and nitrates (Eq. (3)). Further reduction of *ad*NO_x to N_2O involves the removal of O which can be conveniently abstracted by adjacent reduced lattice i.e. Ce^{3+} and the associated oxygen vacancies (Eq. (4)). These reductant sites could either be formed from the reduction of Ce^{4+} by CO (Eqs. (9) and (10)) and/or by formation of nitrites and nitrates (Eqs. (2) and (3)). In fact, N_2O could also form by reducing the chemisorbed NO on reduced ceria–zirconia surface, but as discussed above, its further reduction is limited in the absence of vicinal Cu. Here, the intermolecular reaction between two neighboring adsorbed nitrosyl species is beneficial for the N—N bond formation to yield the related diazo compounds (Eq. (4)).

Dissociation and reduction of chemisorbed NO_x:

At low-temperature region (50–250 °C)

$$Cu^+ + NO \rightarrow Cu^{2+}NO^- \quad (1)$$

$$Cu^{2+}NO^- + Ce^{4+}\text{—}O^- \leftrightarrow Cu^{2+}\text{—}NO_2^- (\text{nitrite}) + Ce^{3+} \quad (2)$$

$$Cu^+\text{—}NO_2 + Ce^{4+}\text{—}O^- \leftrightarrow Cu^{2+}\text{—}NO_3^- (\text{nitrate}) + Ce^{3+} \quad (3)$$

$$2Cu^{2+}NO^- + Ce^{3+} \rightarrow Cu^{2+}\cdots NO^-\cdots NO^-\cdots Cu^{2+} + Ce^{3+} \rightarrow Cu^{2+}N_2O^{2-}Cu^{2+} + Ce^{4+}\text{—}O^- \rightarrow 2Cu^+ + N_2O + Ce^{4+}\text{—}O^- \quad (4)$$

$$Cu^{2+}N_2O^{2-}Cu^{2+} + Ce^{3+} \rightarrow 2Cu^+ + N_2 + Ce^{4+}\text{—}O^- \quad (5)$$

At high-temperature region (>250 °C)

$$Cu^+\text{—}NO + CO + Ce^{3+} \rightarrow Cu^+\text{—}NCO + Ce^{4+}O^- \quad (6)$$

$$Cu^+\text{—}NCO + Cu^+\text{—}NO \rightarrow 2Cu^+ + N_2 + CO_2 \quad (7)$$

$$Cu^+\text{—}NCO + Ce^{4+}O^- \rightarrow Cu^+ + Ce^{3+} + 1/2N_2 + CO_2 \quad (8)$$

Oxidation of carbonaceous species:

$$Ce^{4+}\text{—}O^- + CO \rightarrow Ce^{4+}\text{—}COO^- \rightarrow CO_2 + Ce^{3+} \quad (9)$$

$$Ce^{4+}\text{—}O^- + CO_2 \leftrightarrow Ce^{3+} + \text{carbonate} \quad (10)$$

Further conversion of N_2O to N_2 requires the activation of CO conversion (to CO_2) in a synergistic manner (Eqs. (5) and (10)). At >150 °C, the latter reaction becomes apparent which is in turn dependent on the abundance of reactive lattice oxygen surface sites and their reducibility (Eq. (10)). Between 150 and 250 °C, the rate of N_2O formation decreases gradually as a result of more rapid CO oxidation.

At the higher temperature region (>250 °C), however, the reaction involves NCO intermediate orignating from the interaction of chemisorbed NO and gaseous CO (Eq. (6)), followed by the successive reaction with NO and/or oxygen to yield the N_2 and CO_2 products (Eqs. (7) and (8)). The high reactivity of NCO radical with NO or O_2 was once established by means of kinetic studies [57]. Adsorption of CO_2 and the formation of surface carbonates (Eq. (10)), which was relatively minor at low temperature, becomes the dominant at above 250 °C. The possibility also exists for the formation of O_2^-—Ce^{4+} superoxide species [58], which could interconvert via a sequence of $O_2^- \leftrightarrow O_2^{2-} \rightarrow 2O^-$ at elevated temperature [59] and further contributing to the high-temperature redox on the catalyst surface.

4. Conclusions

In this work, the catalytic *de*NO_x activity of a series of flame synthesized 4% $Cu/Ce_xZr_{1-x}O_2$ (x = 0, 0.25, 0.50, 0.75, 1.0) nanocomposites was studied. The as-prepared catalysts consisted of highly dispersed Cu, with the addition of Zr^{4+} being beneficial for the stabilization of Cu^+ species, presumably through the strong interactions between the two components. The presence of copper and doping with Zr^{4+} (in the form of solid solution) strongly enhances the reactive lattice oxygen content as well as site reducibility, with spillover effects observed during H_2-TPR for all Ce-containing catalysts. The highest surface reducibility was measured for sample $Cu/Ce_{0.75}Zr_{0.25}O_2$.

Based on the results of DRIFT and activity tests, a dissociation mechanism was proposed for the CO + NO reaction at T < 250 °C over $Cu/Ce_xZr_{1-x}O_2$ firstly involving the reductive chemisorption of NO on Cu^+ sites. Here, the coupling nitrosyl species was further dissociated to intermediate N_2O, by reductive Ce^{3+} sites and its associated oxygen vacancies. This is the dominant reaction step at <150 °C. Note that the proposed mechanism for this unusually low-temperature process involves Cu dimmers (Eq. (4)) recently discussed in reference [32]. For the most surface reducible sample of $Cu/Ce_{0.75}Zr_{0.25}O_2$, the activation of CO oxidation over the catalyst at T > 150 °C promoted the rapid formation of N_2, with almost no intermediate N_2O detected beyond 250 °C. Essentially, the *de*NO_x activity was comparable for all Zr-containing catalysts i.e. $Cu/Ce_xZr_{1-x}O_2$ (x < 1.0) likely following an organonitrogen mechanism at temperatures above 250 °C.

Acknowledgments

The financial supports of NSERC through its industrial chair program (R.Z. and S.K.), NSFC (R.Z. and B.C.) with Grant Nos. 20821004, 20877007 and 20977004 and (R.Z.) Program for New Century Excellent Talents in University are greatly acknowledged. The work was partly supported by the ARC through its Centre of Excellence program (W.Y.T. and R.A.).

References

[1] G. Centi, S. Perathoner, Appl. Catal. A 132 (1995) 179.
[2] P. Carniti, A. Gervasini, V.H. Modica, N. Ravasio, Appl. Catal. B 28 (2000) 175.
[3] S. Bennici, A. Gervasini, N. Ravasio, F. Zaccheria, J. Phys. Chem. B 107 (2003) 5168.
[4] M. Fernandez-Garcia, A. Martinez-Arias, J.C. Hanson, J.A. Rodriguez, Chem. Rev. 104 (2004) 4063.
[5] M. Fernandez-Garcia, E.G. Rebollo, A.G. Ruiz, J.C. Conesa, J. Soria, J. Catal. 172 (1997) 146.
[6] W. Shan, W. Shen, C. Li, Chem. Mater. 15 (2003) 4761.
[7] R. Di Monte, J. Kašpar, J. Mater. Chem. 15 (2005) 633.
[8] R.K. Usman, G.W. Graham, W.L.H. Watkins, R.W. McCabe, Catal. Lett. 30 (1995) 53.
[9] A. Bensalem, F.B. Verduraz, M. Delamar, G. Bugli, Appl. Catal. A 121 (1995) 81.
[10] M. Lou, J. Chen, J. Lu, Z. Feng, C. Li, Chem. Mater. 13 (2001) 1491.
[11] A.I. Kozlov, D.H. Kim, A. Yezerets, P. Andersen, H.H. Kung, M.C. Kung, J. Catal. 209 (2002) 417.
[12] W.J. Stark, M. Maciejewski, L. Mädler, S.E. Pratsinis, A. Baiker, J. Catal. 220 (2003) 35.
[13] W.Y. Teoh, R. Amal, L. Mädler, S.E. Pratsinis, Catal. Today 120 (2007) 203.
[14] W.Y. Teoh, R. Setiawan, L. Mädler, J.-D. Grunwaldt, R. Amal, S.E. Pratsinis, Chem. Mater. 20 (2008) 4069.
[15] R. Kydd, W.Y. Teoh, K. Wong, Y. Wang, Q. Zeng, J. Scott, A. Yu, J. Zou, R. Amal, Adv. Funct. Mater. 19 (2009) 369.
[16] L. Mädler, W.J. Stark, S.E. Pratsinis, J. Mater. Res. 17 (2002) 1356.
[17] W.Y. Teoh, L. Mädler, D. Beydoun, S.E. Pratsinis, R. Amal, Chem. Eng. Sci. 60 (2005) 5852.
[18] K.A. Pokrovski, A.T. Bell, J. Catal. 241 (2006) 276.
[19] X. Wang, J.A. Rodriguez, J.C. Hanson, D. Gamarra, A. Martinez-Arias, M. Fernandez-Garcia, J. Phys. Chem. B 110 (2006) 428.
[20] G. Avrouropoulos, T. Ioannides, Appl. Catal. A 244 (2003) 155.
[21] H. Toraya, M. Yashmura, S. Somiya, J. Am. Ceram. Soc. 67 (1984) C119.
[22] J.F. Moulder, W.F. Stickle, P.E. Sobol, K.D. Bomben, Handbook of X-ray Photoelectron Spectroscopy, in: J. Chastain (Ed.), Perkin-Elmer Corporation, Eden Prairie, MN, 1992.
[23] A. Aboukais, A. Bennani, C. Lamonier-Dulongpont, E. Abi-Aad, G. Wrobel, Colloids Surf. A 115 (1996) 171.
[24] G.P. Ansell, A.F. Diwell, S.E. Golunski, J.W. Hayes, R.R. Rajaram, T.J. Truex, A.P. Walker, Appl. Catal. B 2 (1993) 81.
[25] T. Curtin, P. Grange, B. Delmon, Catal. Today 35 (1997) 121.
[26] Y. Wan, J. Ma, Z. Wang, W. Zhou, S. Kaliaguine, J. Catal. 227 (2004) 242.
[27] S. Kaliaguine, A. van Neste, V. Szabo, T.E. Gallot, M. Bassir, R. Muzychuk, Appl. Catal. A 209 (2001) 345.
[28] R. Zhang, A. Villanueva, H. Alamdari, S. Kaliaguine, Appl. Catal. B 64 (2006) 220.
[29] G. Balducci, J. Kašpar, P. Fornasiero, M. Graziani, M. Saiful Islam, J. Phys. Chem. B 102 (1998) 557.
[30] W. Liu, M. Flytzani-Stephanopoulos, Chem. Eng. J. 64 (1996) 283.
[31] L. Kundakovic, M. Flytzani-Stephanopoulos, Appl. Catal. A 171 (1998) 13.
[32] R. Kydd, Ph.D. Thesis, The University of New South Wales, Sydney, 2009.
[33] Y. Chi, S.S.C. Chuang, J. Catal. 190 (2000) 75.
[34] B. Wichterlova, Z. Sobalik, A. Vondrova, Catal. Today 29 (1996) 149.
[35] Y.H. Yeom, M. Li, W.M.H. Sachtler, E. Weitz, J. Catal. 238 (2006) 100.
[36] T. Venkov, K. Hadjiivanov, A. Milushev, D. Klissurski, Langmuir 19 (2003) 3323.
[37] L. Liu, Y. Chen, L. Dong, J. Zhu, H. Wan, B. Liu, B. Zhao, H. Zhu, K. Sun, L. Dong, Y. Chen, Appl. Catal. B 90 (2009) 105.
[38] A.B. Hungria, N.D. Browning, R.P. Erni, M. Fernandez-Garcia, J.C. Conesa, J.A. Perez-Omil, A. Martinez-Arias, J. Catal. 235 (2005) 251.
[39] A. Davydov, IR spectroscopy applied to surface chemistry of oxides, Nauka, Novosibirsk, 1984.
[40] Y. Wan, J. Ma, Z. Wang, W. Zhou, S. Kaliaguine, Appl. Catal. B 59 (2005) 235.
[41] K. Hadjiivanov, Catal. Rev. Sci. Eng. 42 (2000) 71.
[42] J. Szanyi, M. Paffett, J. Catal. 164 (1996) 232.
[43] A. Aylor, S. Larsen, J. Reimer, A.T. Bell, J. Catal. 157 (1995) 592.
[44] R. Zhang, H. Alamdari, S. Kaliaguine, J. Catal. 242 (2006) 241.
[45] J.W. Labdon, A.T. Bell, J. Catal. 31 (1973) 96.
[46] N. Bion, J. Saussey, M. Haneda, M. Daturi, J. Catal. 217 (2003) 47.
[47] O. Gorce, F. Baudin, C. Thomas, P. D. Costa, G. Djéga-Mariadassou, 54 (2004) 69.
[48] M.L. Unland, J. Phys. Chem. 77 (1973) 1952.
[49] K. Almusaiteer, S.C. Chung, J. Catal. 184 (1999) 189.
[50] N. Macleod, R.M. Lambert, Chem. Commun. (2003) 1300.
[51] R. Burch, P.J. Millington, A.P. Walker, Appl. Catal. B 4 (1994) 65.
[52] F. Solymosi, T. Bánsági, J. Catal. 202 (2001) 205.
[53] W.C. Hecker, A.T. Bell, J. Catal. 85 (1984) 389.
[54] R.H.H. Smits, Y. Iwasawa, Appl. Catal. B 6 (1995) L201.
[55] V.I. Pârvulescu, P. Grange, B. Delmon, Catal. Today 46 (1998) 233.
[56] M.C. Kung, H.H. Kung, Top. Catal. 28 (2004) 105.
[57] B. Atakan, J. Wolfrum, Chem. Phys. Lett. 178 (1991) 157.
[58] A. Martinez-Arias, M. Fernandez-Garcia, C. Belver, J.C. Conesa, J. Soria, Catal. Lett. 65 (2000) 197.
[59] R. Zhang, A. Villanueva, H. Alamdari, S. Kaliaguine, J. Mol. Catal. A 258 (2006) 22.